Industrial Chemistry & Materials

ROYAL SOCIETY OF CHEMISTRY

PAPER

View Article Online
View Journal

Cite this: DOI: 10.1039/d6im00026f

Peroxymonosulfate activation with manganese-cobalt sulfide for antibiotic degradation: coupling electron flow modulation and dual reaction pathways

Mengqing Hu,†[ab] Di Zhao,†[b] Xinlong Yan,*[a] Xiaoyan Hu,[a] Xiaofeng Jiang,[a] Shiwei Yin,[c] Ming Zhou[b] and Yun Wang*[b]

Persistent antibiotic pollutants pose significant risks to ecological safety and human health. Developing high-performance catalysts for peroxymonosulfate (PMS) activation is an essential way for efficient antibiotic wastewater remediation. Herein, a three-dimensional nickel foam-supported manganese–cobalt sulfide ($MnCo_2S_4$/NF) catalyst was synthesized and employed to activate PMS for sulfamethoxazole (SMX) degradation. The $MnCo_2S_4$/NF/PMS system achieved 87.7% SMX removal within 20 minutes and maintained over 82% efficiency after seven consecutive cycles, demonstrating excellent catalytic activity and stability. Density functional theory (DFT) studies revealed that the metallic nature of $MnCo_2S_4$ facilitates strong PMS adsorption, which facilitates electron transfer from the catalyst to PMS and promotes O–O bond cleavage. Specifically, Mn sites act as the primary electron-donating centers, while Co sites synergistically reduce charge-transfer resistance. Quenching experiments and electron paramagnetic resonance (EPR) analysis confirmed that superoxide radical ($^{\bullet}O_2^-$) and non-radical singlet oxygen ($^1O_2$) synergistically contributed to SMX degradation. Fukui function analysis further identified a pronounced susceptibility of the nitrogen atom (N7) of SMX to electrophilic radical attack, as well as the critical involvement of specific carbon atoms (*e.g.*, C1, C5) in nucleophilic interactions. Moreover, this system demonstrates excellent performance across various water matrices, showing its strong potential for practical water treatment.

Received 20th January 2026,
Accepted 22nd April 2026

DOI: 10.1039/d6im00026f

rsc.li/icm

Keywords: Peroxymonosulfate activation; Manganese–cobalt sulfide; Sulfamethoxazole degradation; AOPs.

1 Introduction

The widespread occurrence of antibiotics in aquatic environments has emerged as a significant global environmental concern, as it not only disrupts ecological balance but also poses a serious threat to human health through the promotion of antimicrobial resistance.[1,2] Sulfamethoxazole (SMX), a frequently prescribed sulfonamide antibiotic, is commonly detected in surface waters, groundwater, and effluents from wastewater treatment plants due to its high aqueous solubility, chemical stability, and persistent antibacterial activity.[3,4] Conventional wastewater treatment technologies, including activated sludge processes and biofiltration, exhibit limited efficiency in removing SMX, leading to its continuous accumulation in the environment.[5,6] Therefore, there is a pressing need to develop more efficient and sustainable treatment strategies to mitigate this issue.

In recent years, peroxymonosulfate (PMS)-based advanced oxidation processes (AOPs) have garnered considerable attention as a promising approach for the effective degradation of recalcitrant organic pollutants.[7–9] The asymmetric structure of HSO_5^- facilitates its activation, and combined with high redox potential (1.82 V) and excellent performance in near-neutral conditions, it makes PMS a highly effective choice for treating complex wastewater matrices.[10] Heterogeneous transition-metal catalysts activate PMS to enable the *in situ* generation of a spectrum of highly reactive oxygen species (ROS), such as hydroxyl radicals ($^{\bullet}OH$), sulfate radicals ($^{\bullet}SO_4^-$), and superoxide radicals ($^{\bullet}O_2^-$), which act synergistically to drive rapid and efficient oxidative degradation of organic contaminants.[10] Notably, beyond these species, other essential ROS, such as singlet oxygen ($^1O_2$), also contribute significantly

[a] *Jiangsu Province Engineering Research Center of Fine Utilization of Carbon Resources, School of Chemical Engineering & Technology, China University of Mining and Technology, Xu Zhou 221116, P.R. China. E-mail: yanxl@cumt.edu.cn*
[b] *School of Environment and Science, Gold Coast Campus, Griffith University, Gold Coast, QLD 4222, Australia. E-mail: yun.wang@griffith.edu.au*
[c] *Key Laboratory for Macromolecular Science of Shaanxi Province, School of Chemistry and Chemical Engineering, Shaanxi Normal University, Xi'an 710119, P. R. China*
† These authors contributed equally to this work.

to pollutant degradation, enabling a versatile radical and non-radical coupling mechanism.[11,12] This multi-oxidative capacity positions PMS-based AOPs as a robust and adaptable solution for environmental remediation.

The efficiency of PMS activation is critically influenced by the choice of catalysts. Transition metal-based catalysts, such as those incorporating cobalt and manganese, have demonstrated outstanding performance in PMS activation due to their favorable redox properties.[13–15] Metal sulfides demonstrate a notable advantage in activating PMS for pollutant degradation, primarily due to their superior electronic properties and the role of their sulfur constituents.[16,17] Specifically, the low band gap energy inherent to the sulfide of spinel structure, such as cobalt manganese sulfide, significantly enhances their electrical conductivity by up to two orders of magnitude compared to their oxide counterparts.[18] This superior conductivity is crucial for catalytic processes, particularly in PMS activation, where efficient electron transfer from the catalyst to PMS molecules is often the rate-limiting step for O–O bond cleavage and subsequent reactive species generation.[15,19] Consequently, such high conductivity directly translates to accelerated reaction kinetics and enhanced catalytic efficiency. This improvement in metal sulfide performance is also closely linked to the fundamental properties of sulfur. Sulfur possesses a lower electronegativity than oxygen, which not only facilitates the redox cycling of metal ions but also actively participates in electron transfer pathways, thereby accelerating active species generation.[20] For instance, Han *et al.*[21] demonstrated that MnS achieved complete degradation of levofloxacin (LVF) within 45 minutes by PMS activation, a performance significantly superior to that of Mn_2O_3, which only yielded approximately 70.1% LVF removal. This enhanced activity in MnS was attributed to its superior electrical conductivity and more facile electron transfer, as supported by DFT calculations showing a higher Fermi level for α-MnS compared to α-Mn_2O_3. Similarly, Zhao *et al.*[17] reported that the CoS/PMS system achieved a remarkable 100% removal efficiency of tetracycline (TC) within just 1 min, highlighting its exceptional catalytic prowess. Thus, metal sulfides exhibit significant potential for activating PMS in the degradation of antibiotic contaminants.

Although these materials possess excellent inherent catalytic activity, conventional powder-form catalysts often suffer from difficult separation and poor recoverability, thereby restricting their broader practical implementation.[22,23] A solution involves immobilizing these catalysts onto three-dimensional (3D) nickel foam (NF) scaffolds, which offer robust mechanical stability and minimal powder loss, coupled with ease of catalyst separation and reuse, contributing to longer catalyst life and reduced costs.[24] These features collectively confer distinct advantages for practical applications in water treatment systems, including simplified catalyst exchange without hazardous dust and full recoverability, enhancing sustainability. Compared to monometallic or powder-form catalysts, the 3D NF-supported bimetallic sulfide offers distinct advantages. The metallic-like conductivity of the spinel sulfides accelerates electron transfer between the catalyst surface and PMS. Additionally, its integrated structure avoids secondary pollution and eliminates the difficulties of catalyst recovery.

In this study, a 3D NF-supported $MnCo_2S_4$ catalyst ($MnCo_2S_4$/NF) was fabricated and used to activate PMS, enabling efficient SMX degradation. The effects of key operational parameters, including catalyst dose, PMS concentration, solution pH, and temperature, on the degradation performance were systematically investigated. Density functional theory (DFT) studies confirmed the strong PMS adsorption ability of $MnCo_2S_4$/NF, promoting electron transfer and O–O bond cleavage. Fukui function analysis revealed that the nitrogen atom (N7) in SMX is highly vulnerable to electrophilic attack, specific carbon atoms such as C1 and C5, are involved in nucleophilic interactions, highlighting the synergistic roles of radical ($^{\cdot}O_2^-$) and non-radical ($^1O_2$) pathways in SMX degradation. This work advances the understanding of antibiotic degradation in PMS-based AOPs. It uses DFT and Fukui analysis to reveal enhanced electron transfer from spinel sulfides and clarify SMX degradation pathways. These insights support sustainable water treatment and provide a practical framework for efficient wastewater management.

2 Results and discussion

2.1 Characterization

The synthesis process of 3D porous $MnCo_2S_4$/NF is shown in Fig. 1a, the two-step hydrothermal synthesis followed by high-temperature annealing to grow $MnCo_2S_4$ directly on NF. First, Mn^{2+} and Co^{2+} precursors are co-deposited onto the NF substrate *via* hydrothermal treatments. Subsequent sulfidation and annealing convert this intermediate into crystalline $MnCo_2S_4$, which adheres *in situ* to the NF skeleton, producing an integrated, mechanically robust catalyst with abundant pore networks. The phase composition and crystallinity of $MnCo_2S_4$/NF were examined by XRD. As shown in Fig. 1b, the strong reflections at 2θ = 44.52°, 52.44°, and 76.35° correspond to the (111), (200), and (220) planes of the Ni substrate (JCPDS No. 87-0712),[25] respectively, masking residual peaks from the Mn/Co precursor. After sulfidation, additional peaks at 2θ = 31.2°, 36.7°, 49.9°, and 55.3° emerge and can be indexed to the (311), (400), (511), and (440) planes of cubic $MnCo_2S_4$ (isostructural with Co_3S_4, JCPDS No. 73-1703), confirming successful phase transformation and enhanced crystallinity.[26] In $MnCo_2S_4$, Mn substitutes for Co in the Co_3S_4 lattice without altering the crystal structure, resulting only in slight changes to the lattice parameters.[27] Nitrogen adsorption–desorption isotherms (Fig. 1c) reveal that $MnCo_2S_4$/NF exhibits a type IV profile with pronounced hysteresis loops, indicative of micro- and mesoporosity. The BET surface area of the NF-supported catalyst (Table S1) is lower than that of equivalent powdered materials. This reduction is likely attributed to the direct growth of the catalyst on the NF, primarily reflecting the dominant mass contribution of the macroporous NF substrate.[28] The catalytic excellence is not derived from high BET surface area, but rather from the highly accessible active centers and the intrinsic metallic properties of the $MnCo_2S_4$ crystals. The average pore

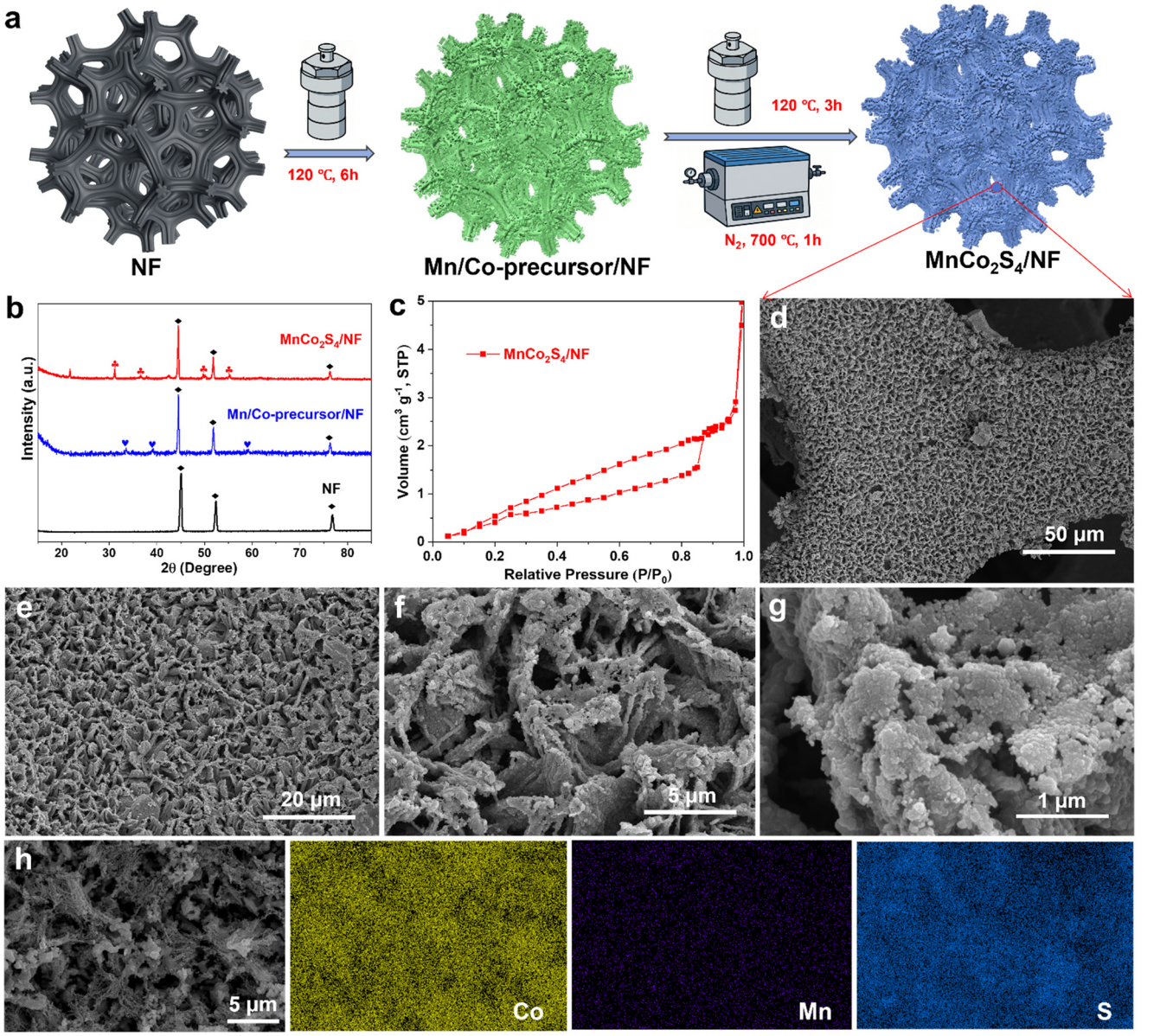

Fig. 1 (a) Schematic diagram of the synthesis route of $MnCo_2S_4$/NF; (b) XRD patterns and (c) nitrogen sorption isotherms of $MnCo_2S_4$/NF; SEM images of (d–g) and (h) corresponding element mapping images of $MnCo_2S_4$/NF.

diameter of 10.9 nm lies within the mesoporous regime, facilitating rapid PMS diffusion and activation, thereby maximizing the availability of active sites for efficient pollutant degradation.[29] Subsequently, the morphology and composition of the synthesized $MnCo_2S_4$/NF were further characterized. As shown in Fig. S2, the pristine nickel foam exhibits a smooth surface with a well-defined three-dimensional porous architecture. SEM images of $MnCo_2S_4$ grown on NF (Fig. 1d–g) reveal a hierarchical porous structure spanning both the micro- and nanoscale. Furthermore, we compared SEM images of samples at different calcination temperatures, revealing significant morphological changes during heat treatment (Fig. S3). At lower temperatures (300 °C and 500 °C), the surface was primarily covered with relatively thin nanosheets. Increasing the calcination temperature to 700 °C promoted grain growth and structural reorganization, ultimately forming a robust, hierarchical dendritic structure composed of interconnected nanoparticles. Compared with the precursor material (Fig. S4), the sulfidized surface exhibited pronounced wrinkling. This transformation, facilitated by optimized high-temperature calcination at 700 °C, enabled more complete sulfidation and produced the characteristic hierarchical dendritic morphology of high-performance sulfides, while preserving the overall structural integrity of the parent precursor. This unique structure increases the specific surface area and exposes a higher density of active sites, which is favorable for the catalytic activation of PMS in pollutant degradation. Therefore, all subsequent experiments were conducted using samples calcined at 700 °C. Additionally, elemental mapping by energy-dispersive spectroscopy (EDS) (Fig. 1h) confirms the uniform

distribution of Co, Mn, and S throughout the material, indicating homogeneous composition without observable phase segregation, ensuring the stability and consistent performance. The metal distribution is further quantified by ICP-MS analysis (Table S2), which determines in the $MnCo_2S_4$/NF catalyst, to be 9.59% for Co and 4.69% for Mn. The measured Co/Mn mass ratio is approximately 2.04, which is in close agreement with the theoretical stoichiometric ratio of the $MnCo_2S_4$ spinel phase. The high Ni content (47.25%) originates from the metallic nickel foam substrate. Thus, these characterizations ensure the structural stability and consistent catalytic performance of the synthesized material.

The elemental composition and surface chemical states of the $MnCo_2S_4$/NF catalyst were investigated by XPS. The full survey spectrum (Fig. S5) confirms the presence of Mn, Co, S, and O elements in the sample. High-resolution Co 2p spectra exhibit characteristic peaks at 780.3 eV and 795.7 eV, corresponding to Co^{3+} $2p_{3/2}$ and $2p_{1/2}$, respectively, while peaks at 783.1 eV and 798.1 eV are assigned to Co^{2+} (Fig. 2a).[30,31] Compared to the Co 2p spectrum of the precursor, $MnCo_2S_4$/NF shows a stronger Co^{3+} signal and a reduced Co^{2+} contribution, indicating that the sulfidation process promotes the oxidation of Co^{2+} to Co^{3+}. The Mn 2p spectrum displays peaks at 643.4 eV and 641.3 eV, which are attributed to Mn^{3+} and Mn^{2+}, respectively (Fig. 2b).[32] The relative intensity suggests a higher proportion of Mn^{2+} in $MnCo_2S_4$/NF compared to the precursor. The coexistence of Mn and Co in multiple oxidation states is beneficial for redox cycling during PMS activation. The O 1 s spectrum can be deconvoluted into two main components, including lattice oxygen (O_L) at higher binding energies and adsorbed oxygen (O_{Ad}) at lower binding energies (Fig. 2c).[33] The enhanced O_{Ad} signal after sulfidation indicates an increased presence of surface defects or hydroxyl groups, which can serve as active sites for PMS adsorption and activation. This enhancement facilitates reactive oxygen species (ROS) generation, contributing to the efficient degradation of SMX. Furthermore, the S 2p spectrum reveals distinct peaks at 162.2 eV (S $2p_{3/2}$) and 164.5 eV (S $2p_{1/2}$), confirming the presence of sulfide species (S^{2-}) within the spinel lattice (Fig. 2d).[34] These sulfide ions act as electron donors, promoting the redox cycling of Mn and Co, enhancing the stability of the catalyst, and improving both durability and catalytic reactivity.[35,36]

2.2 Catalytic performance of $MnCo_2S_4$/NF

The catalytic performance of the synthesized $MnCo_2S_4$/NF was systematically evaluated by monitoring the degradation of SMX. As illustrated in Fig. 3a, the degradation efficiencies of SMX

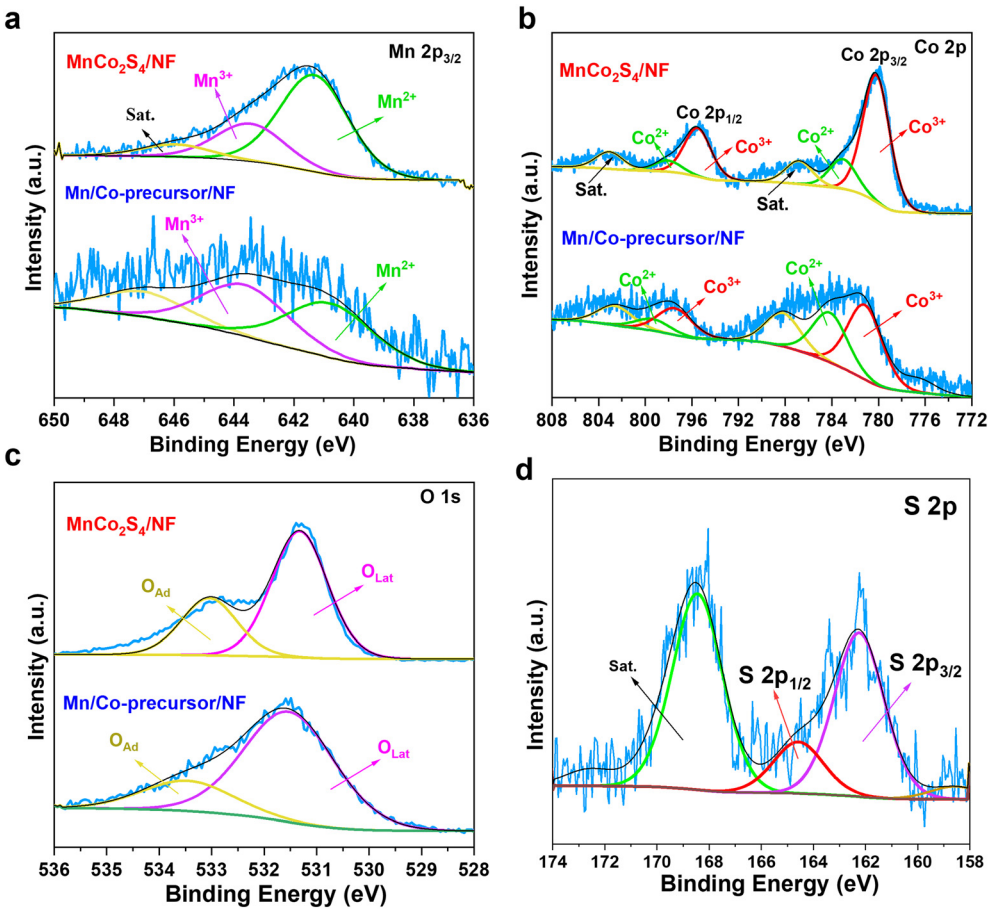

Fig. 2 High-resolution XPS spectra of (a) Co, (b) Mn, (c) O, and (d) S for $MnCo_2S_4$/NF and Co/Mn-precursor/NF.

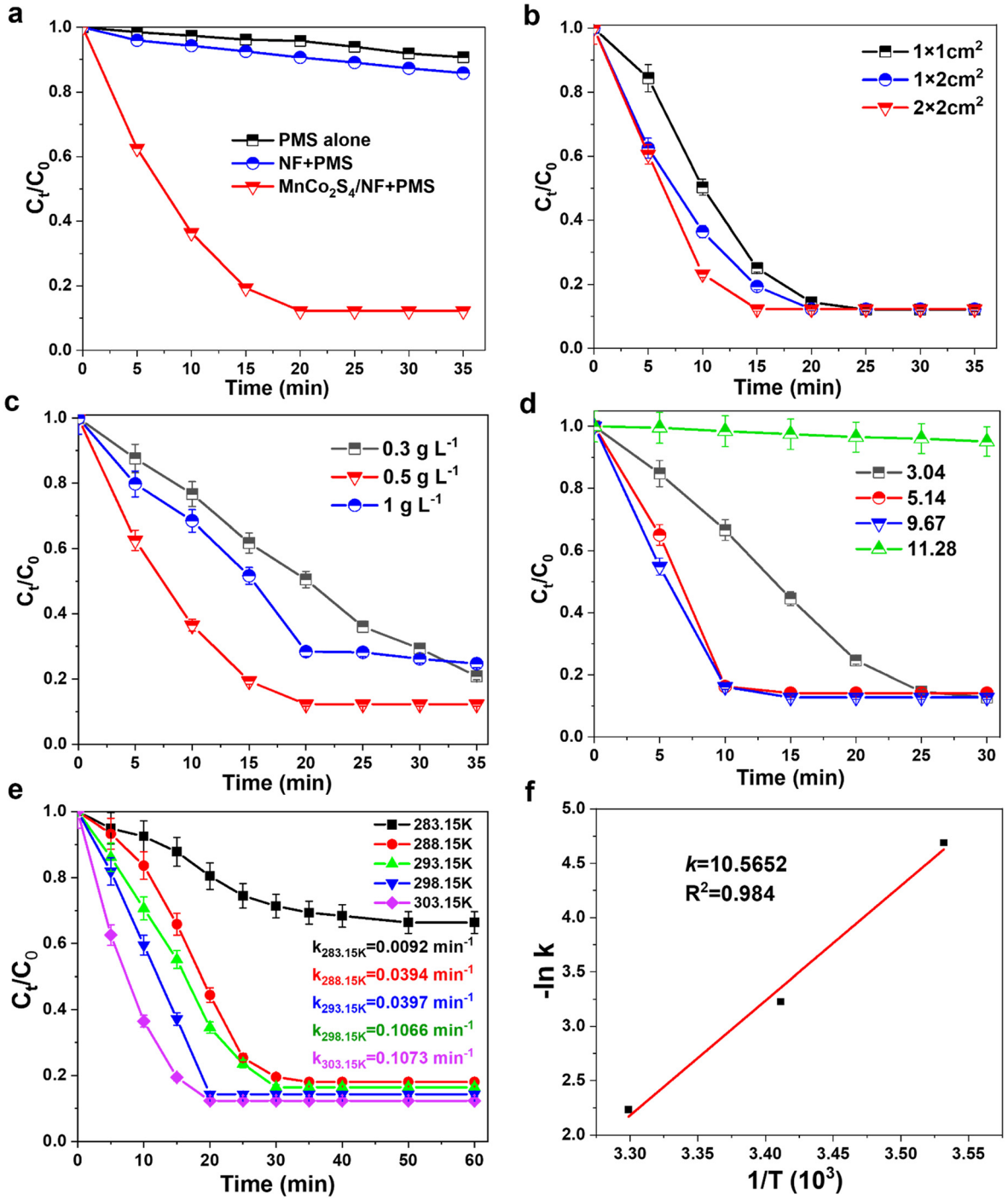

Fig. 3 (a) SMX degradation efficiencies by various catalyst systems; influence of (b) catalyst dosage, (c) PMS concentration, and (d) pH on SMX degradation; SMX degradation efficiencies at (e) varying temperatures and (f) Arrhenius equation linear fitting.

across different reaction systems are compared. In the presence of PMS alone, only limited degradation of SMX (9%) was observed, primarily attributed to the mild self-activation of PMS at the experimental temperature of 30 °C. In the NF/PMS system, the SMX removal efficiency remained below 15%, indicating that NF alone lacks the capacity to effectively activate PMS for SMX degradation. Obviously, the $MnCo_2S_4$/NF/PMS system achieved a significantly enhanced degradation efficiency of 87.7% within 20 minutes, highlighting the superior catalytic activity of $MnCo_2S_4$/NF. To further elucidate the interfacial reaction kinetics, the Langmuir–Hinshelwood (L–H) model was applied to analyze the experimental data (Fig. S6 and Table S3). The degradation of SMX over $MnCo_2S_4$/NF exhibited a high correlation with the L–H model, yielding an intrinsic reaction rate constant (k_r) of 3.738 mg L^{-1} min^{-1} and an adsorption coefficient K_{ads} of 0.0325 L mg^{-1}. This kinetic behavior confirms

that the catalytic process is governed by the adsorption–reaction–desorption cycle on the catalyst surface. The observed curvature in the C_t/C_0 plots, characterized by a rapid initial decay followed by a slower decline, is a hallmark of the L–H mechanism, stemming from the competitive occupancy of active sites between SMX molecules and the accumulating degradation intermediates. A comparable removal performance was observed in the Co/Mn-precursor/NF/PMS system. However, the poor stability and limited reusability of the precursor material (Fig. S7) restrict its practical application. The precursor catalyst without high-temperature treatment may undergo severe surface passivation in the strongly oxidizing PMS environment and experience a rapid loss of active components due to weak interfacial bonding, resulting in poor cycling stability and a marked decline in degradation performance. Moreover, compared with previously reported catalysts, the synthesized $MnCo_2S_4$/NF exhibits superior SMX degradation performance, achieving higher removal capacity within a shorter time and at a lower catalyst dosage (Table S4).

Further influencing factors were also investigated. As shown in Fig. 3b and Table S5, increasing the catalyst area from 1 cm^2 to 4 cm^2 resulted in a marked improvement in degradation performance. This enhancement is attributed to the increase in available active sites, which facilitates the participation of more metal centers in PMS activation, thereby generating a greater quantity of reactive oxygen species (ROS) such as $^{\bullet}SO_4^-$ and $^{\bullet}OH$, accelerating SMX decomposition. Fig. 3c and Table S6 depict the effect of PMS concentration on SMX degradation. An increase in PMS concentration from 0.3 g L^{-1} to 0.5 g L^{-1} significantly boosted degradation efficiency due to the higher availability of ROS. However, a further increase to 1.0 g L^{-1} led to a decline in SMX removal. This reduction may be due to the excessive PMS reacting with the generated $^{\bullet}SO_4^-$ and $^{\bullet}OH$ radicals (as described in eqn (1) and (2)), resulting in their consumption and promoting the disproportionation of sulfate radicals (eqn (3)), ultimately diminishing the oxidative capacity. Therefore, the optimal PMS concentration for this catalytic system was determined to be 0.5 g L^{-1}.

$$\cdot SO_4^- + S_2O_8^{2-} \rightarrow SO_4^{2-} + \cdot S_2O_8^- \quad (1)$$

$$\cdot OH + S_2O_8^{2-} \rightarrow OH^- + \cdot S_2O_8^- \quad (2)$$

$$\cdot SO_4 + \cdot SO_4^- \rightarrow \cdot S_2O_8^{2-} \quad (3)$$

The influence of pH on SMX degradation was also examined, as pH plays a pivotal role in determining the speciation of reactive radicals in AOPs. The degradation efficiency of SMX by the $MnCo_2S_4$/NF-activated PMS system was evaluated under varying pH conditions (Fig. 3d). As the pH increased from 3 to 9.67, the degradation performance improved progressively. However, further increase to pH 11.28 resulted in a sharp decline in removal efficiency, with the first-order rate constant decreasing to 0.0018 min^{-1} (Table S7), consistent with previous findings. Under mildly acidic to near-neutral pH, PMS primarily exists as HSO_5^-, while excess hydrogen ions scavenge sulfate and hydroxyl radicals (eqn (4) and (5)), reducing the efficiency of the oxidation process. Conversely, under strongly alkaline conditions, PMS decomposes non-radically into SO_4^{2-} and O_2, suppressing ROS generation. Moreover, an abundance of OH^- can quench $^{\bullet}SO_4^-$ radicals (eqn (6)–(8)), further impeding the degradation process.

$$\cdot OH + H^+ + e^- \rightarrow H_2O \quad (4)$$

$$SO_4^{2-} + H^+ + e^- \rightarrow \cdot HSO_4^- \quad (5)$$

$$HSO_5^- + H_2O \rightarrow SO_5^{2-} + OH^- \quad (6)$$

$$HSO_5^- + SO_5^{2-} \rightarrow HSO_6^- + SO_4^{2-} \quad (7)$$

$$HSO_6^- + OH^- \rightarrow H_2O + SO_4^{2-} + O_2 \quad (8)$$

To elucidate the effect of temperature on PMS activation and SMX degradation, a series of experiments was conducted across a temperature gradient. The results demonstrated a pronounced enhancement in catalytic activity with increasing temperature (Fig. 3e). As the temperature increased from 283.15 K to 303.15 K, the observed rate constant (k_{obs}) increased from 0.0092 min^{-1} to 0.1073 min^{-1}, indicating that higher temperatures facilitate PMS activation and enhance ROS generation. Additionally, elevated temperatures intensify molecular motion on the catalyst surface, further accelerating the reaction kinetics. The apparent activation energy (E_a) was calculated to be 87.83 kJ mol^{-1} based on the Arrhenius equation by plotting the logarithm of the rate constant against the reciprocal of temperature (Fig. 3f).

2.3 Catalytic mechanism of $MnCo_2S_4$/NF catalyst

To clarify the degradation mechanism of SMX through PMS activation, we systematically examined the formation and functions of reactive oxygen species (ROS). Quenching experiments were carried out to determine the types of ROS generated in the $MnCo_2S_4$/NF-activated PMS system (Fig. 4a). Without the addition of any quenching agents, the SMX removal efficiency reached 87.7% within 30 minutes. Upon the addition of 100 mM methanol or 50 mM *tert*-butyl alcohol (TBA), common quenchers for both hydroxyl radicals ($^{\bullet}OH$) and sulfate radicals ($^{\bullet}SO_4^-$), the SMX removal rates declined to 65% and 79%, respectively. Corresponding kinetic data fitting revealed apparent rate constants (k_{obs}) of 0.0500 min^{-1} for methanol and 0.0503 min^{-1} for TBA (Fig. 4b). These values are notably lower than the k_{obs} of 0.1073 min^{-1} observed without any quencher, indicating a reduction of approximately 0.057 min^{-1}. However, this modest decrease suggests that $^{\bullet}SO_4^-$ and $^{\bullet}OH$ play only a minor role in the degradation of SMX in this system. In contrast, when 5 mM *p*-benzoquinone (*p*-BQ), a scavenger of superoxide anion radicals ($^{\bullet}O_2^-$), and L-histidine, a specific quencher for singlet oxygen ($^1O_2$), were introduced, the degradation efficiency was significantly inhibited. The SMX

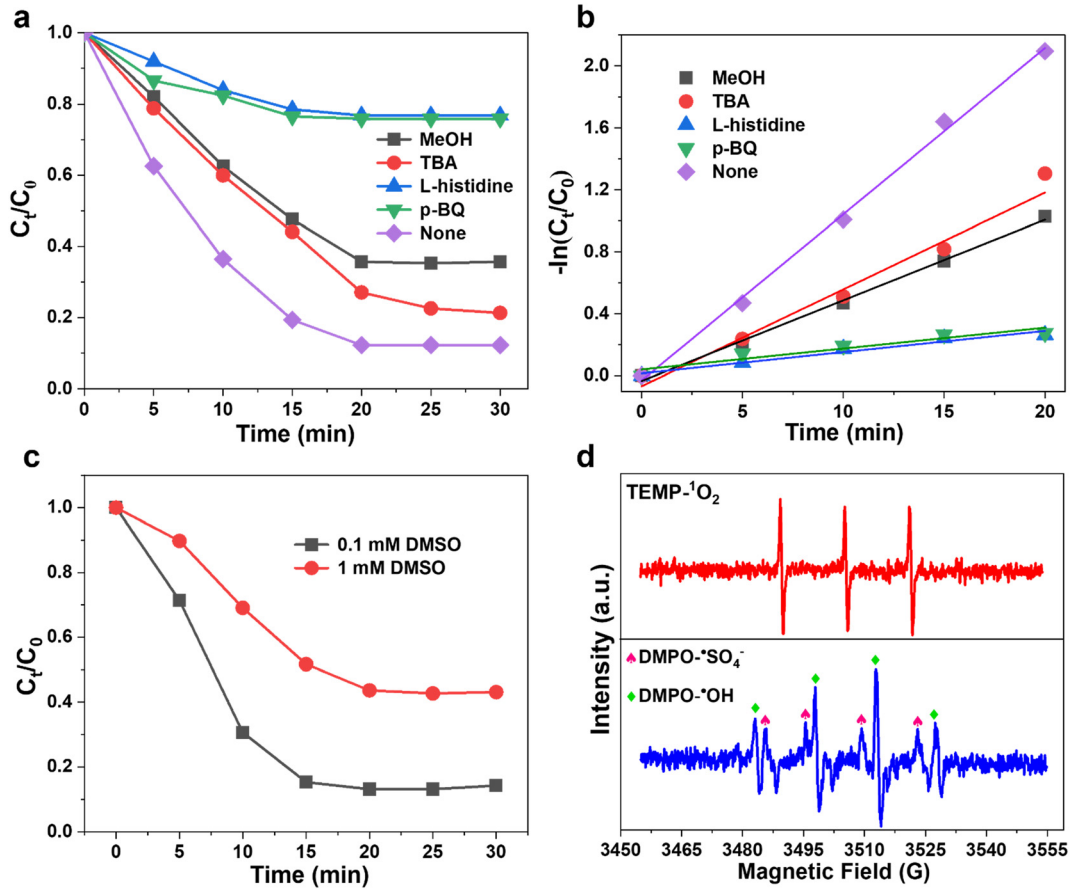

Fig. 4 (a–c) Impact of radical scavengers on SMX degradation in $MnCo_2S_4$/NF/PMS systems; (d) EPR spectroscopy analysis of $^{\bullet}OH$ and $^{\bullet}SO_4^-$ and $^1O_2$ in the $MnCo_2S_4$/NF/PMS systems.

removal dropped to 24.1% and 22.3%, respectively, within 30 minutes. Kinetic analysis revealed that k_{obs} decreased to 0.0177 min^{-1} with *p*-BQ and 0.0163 min^{-1} with L-histidine. These results indicate that $^1O_2$ is the predominant ROS responsible for SMX degradation in the system, and $^{\bullet}O_2^-$ also plays a critical role. It is important to note that both methanol and TBA are hydrophilic and thus exhibit limited interaction with the catalyst surface, meaning they primarily quench free radicals in the aqueous phase rather than those bound to the catalyst surface. To evaluate the contribution of surface-bound ROS, dimethyl sulfoxide (DMSO), which can penetrate the catalyst interface, was employed as a quencher (Fig. 4c). The addition of 0.1 mM DMSO reduced the degradation efficiency to 67% within 20 minutes, while 1 mM DMSO further decreased it to 56.34%. These results suggest that surface-bound ROS have a relatively minor, yet non-negligible, role in SMX degradation within the $MnCo_2S_4$/NF/PMS system. The quenching experiments confirm the presence and participation of multiple ROS, and the degradation of SMX proceeds *via* both radical ($^{\bullet}O_2^-$) and non-radical ($^1O_2$) pathways. To further identify the specific species involved, *in situ* electron paramagnetic resonance (EPR) spectroscopy was conducted (Fig. 4d). In the $MnCo_2S_4$/NF/PMS system, a characteristic 1 : 1 : 1 triplet signal with strong intensity was observed, attributable to singlet oxygen ($^1O_2$) generated from PMS decomposition. This observation is consistent with the L-histidine quenching results, further substantiating the critical role of $^1O_2$ in PMS activation by the bimetallic sulfide catalyst. Additionally, EPR spectra detected spin-adduct signals corresponding to both DMPO–$^{\bullet}SO_4^-$ and DMPO–$^{\bullet}OH$ (1 : 2 : 2 : 1 quartet pattern),[37,38] confirming the formation of these radical species, although their contributions to SMX degradation appear limited.

To gain deeper insights into the role of $MnCo_2S_4$/NF in PMS activation, DFT calculations were conducted. As shown in Fig. 5a and b, upon adsorption of PMS onto the $MnCo_2S_4$/NF catalyst, the O–O bond length increased significantly from 1.151 Å to 2.961 Å, suggesting bond cleavage. The calculated adsorption energy of PMS on $MnCo_2S_4$/NF (E_{ad}–PMS) was −3.06 eV, indicating a strong interaction between PMS and the catalyst surface that promotes its activation and subsequent decomposition. This strong interaction is closely correlated with the metallic nature of $MnCo_2S_4$, as evidenced by the spin-up and spin-down total density of states (TDOS) shown in Fig. 5d. The TDOS exhibits a non-zero value at the Fermi level (EF), indicating that there is no band gap near the Fermi region. The continuous distribution of electronic states across EF confirms the metallic nature of this material, which is conducive to high electron

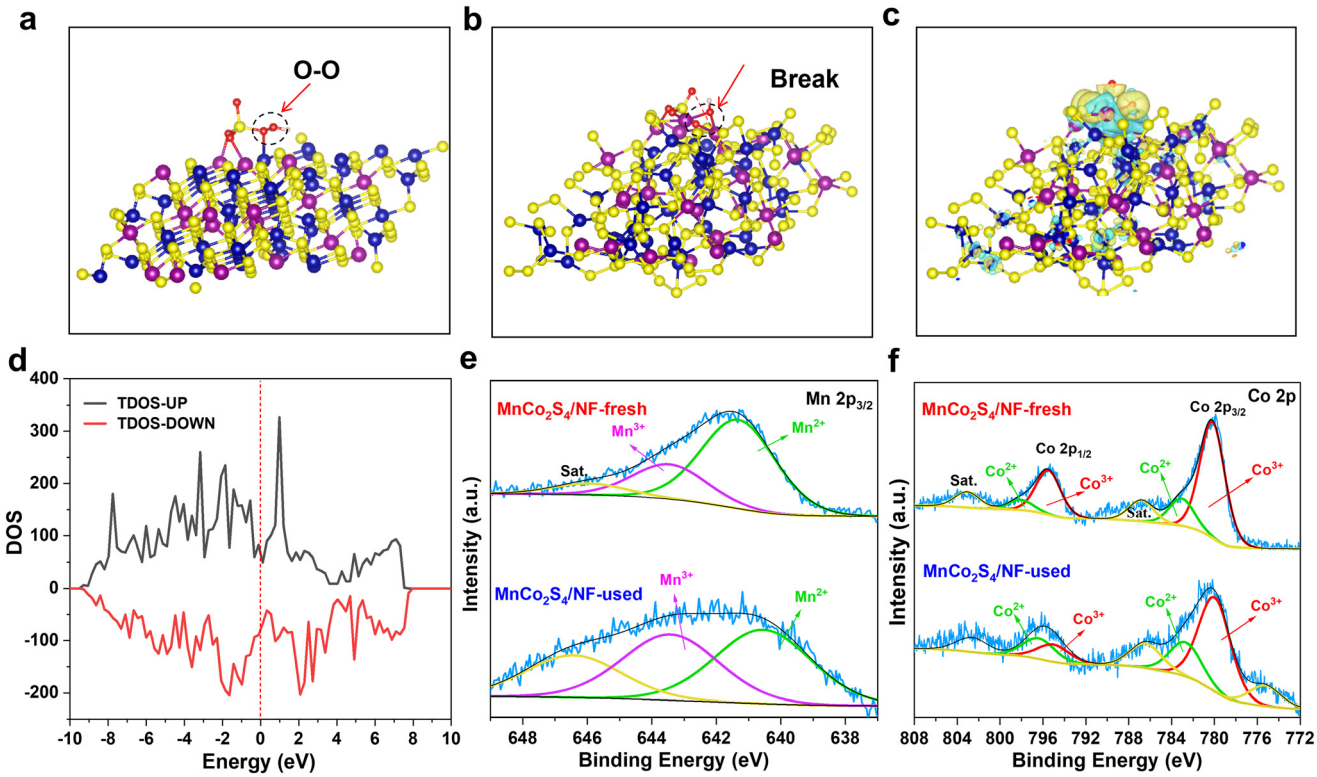

Fig. 5 Structure diagram of PMS adsorption on the active site of $MnCo_2S_4$/NF catalyst (a) before and (b) after geometric optimization; (c) electron density distribution for PMS adsorption on the active sites of $MnCo_2S_4$/NF catalyst (yellow regions denote areas of high electron density, while blue regions signify areas of low electron density); (d) total and partial density of state (DOS) for $MnCo_2S_4$; (e) high-resolution XPS spectra of Mn and Co (f) for $MnCo_2S_4$/NF before and after SMX degradation.

mobility. This theoretical prediction of conductivity is further validated by the electrochemical impedance spectroscopy (EIS) measurements (Fig. S8). As illustrated in the Nyquist plots, the $MnCo_2S_4$/NF catalyst exhibits a significantly smaller semicircle diameter compared to its oxide-based precursor. This reduction in the charge transfer resistance (R_{ct}) confirms that the modulated electronic structure of the bimetallic sulfide facilitates faster interfacial electron shuttling. As shown in Fig. 5c, charge density difference analysis reveals substantial electron accumulation on the PMS molecule (yellow regions), corresponding to a net charge transfer of 2.20e from $MnCo_2S_4$/NF to PMS. Further site-specific charge analysis indicates that Mn serves as the primary electron-donating active site, with three adjacent Mn transferring 0.79e, 1.10e, and 0.78e to PMS, respectively. In contrast, the Co site exhibits negligible charge variation (0.03e) before and after adsorption, but Co may facilitate Mn-site regeneration through bimetallic synergy, thereby reducing interfacial charge-transfer resistance and accelerating electron transport. In addition, XPS was employed to analyze the chemical valence states of the $MnCo_2S_4$/NF catalyst before and after the reaction. As shown in Fig. 5e and f, the XPS characteristic peaks of Co 2p and Mn 2p were examined. After the reaction, a decrease in Mn^{2+} content and a corresponding increase in Mn^{3+} were observed, while Co^{2+} content slightly increased and Co^{3+} content decreased. These changes indicate the presence of Co^{3+}/Co^{2+} and Mn^{2+}/Mn^{3+} redox cycles.[39] Thus, the coexistence of Mn and Co induces a synergistic effect, forming a coupled redox system that enhances the catalytic activation of PMS and facilitates the generation of ROS.[40] Additionally, the sulfide framework contributes to structural stability and supports electron transfer.[41] Based on these findings, a mechanism for PMS activation and ROS generation in the $MnCo_2S_4$/NF system is proposed. PMS is activated through valence state transitions of Mn, where the formation of $^{\cdot}SO_4^-$ and OH^- is mainly driven by Mn^{2+} (eqn (9)). To validate the proposed reaction pathway, the reaction energies (ΔE) of various PMS dissociation routes were calculated (Fig. 6a and b, and Table S8). PMS decomposition at the Mn site is energetically favorable for the formation of $^{\cdot}SO_4^-$and M–OH, after which the adsorbed M–OH preferentially converts to OH^-. This indicates that the generation of $^{\cdot}SO_4^-$and OH^- is the initial step of the PMS activation process. Moreover, Co^{2+} reduces Mn^{3+} *via* internal electron transfer while being oxidized to a higher valence state, which is subsequently reduced and regenerated by PMS. Notably, the $^{\cdot}SO_5^-$ species generated during this process does not significantly contribute to oxidative degradation due to its low redox potential (eqn (9)–(11)).

$$Mn^{2+} + HSO_5^- \rightarrow Mn^{3+} + \cdot SO_4^- + OH^- \quad (9)$$

$$Mn^{3+} + Co^{2+} \rightarrow Mn^{2+} + Co^{3+} \quad (10)$$

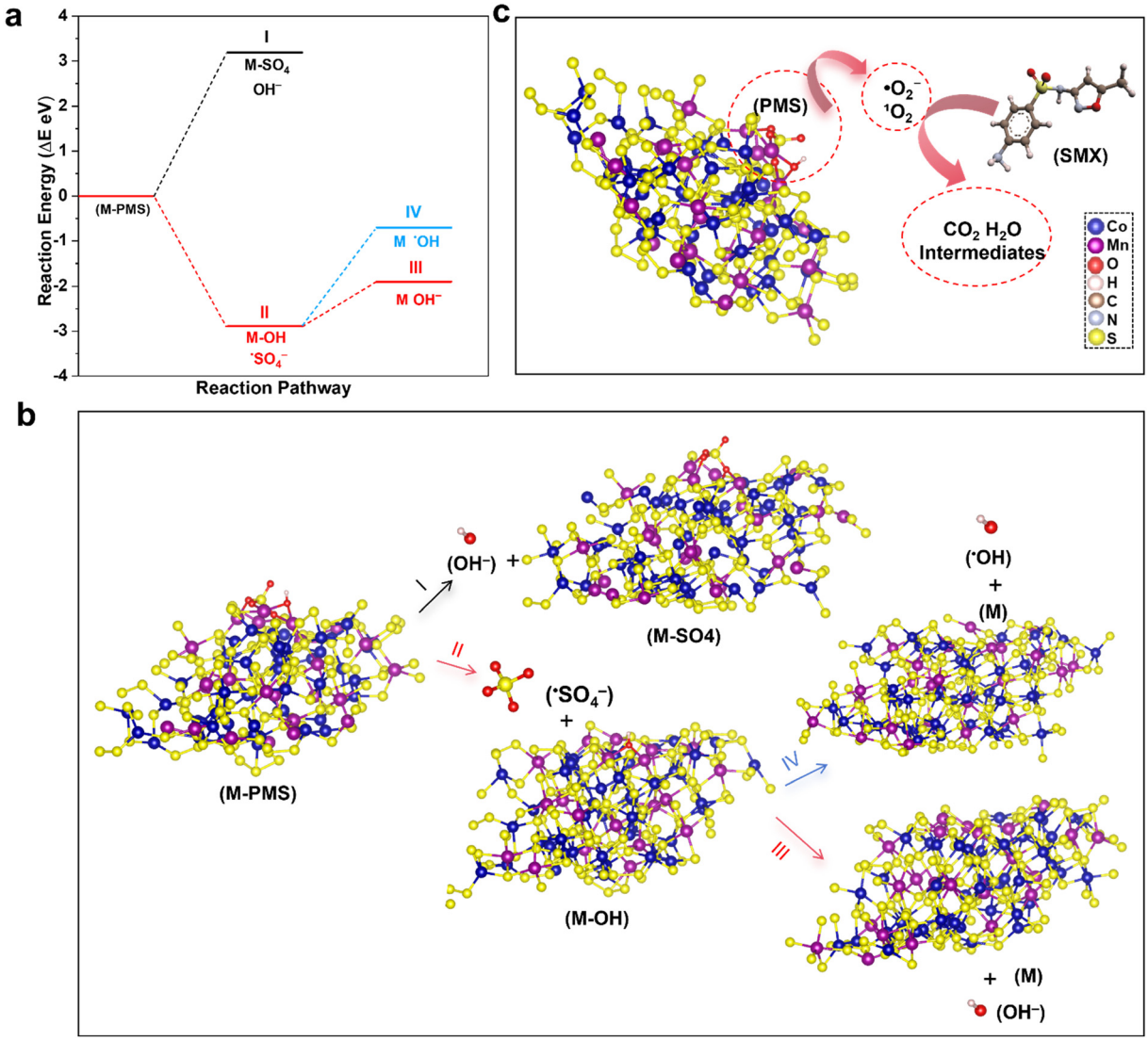

Fig. 6 (a and b) Reaction energy (ΔE) comparison of $MnCo_2S_4$/NF catalysts for different proposed reaction pathways; (c) proposed mechanism of SMX degradation in the $MnCo_2S_4$/NF system.

$$Co^{3+} + HSO_5^- \rightarrow Co^{2+} + \cdot SO_5^- + H^+ \quad (11)$$

Secondly, $^{\cdot}OH$ can be produced through the consumption of $^{\cdot}SO_4^-$ (eqn (12) and (13)).

$$\cdot SO_4^- + OH^- \rightarrow SO_4^{2-} + \cdot OH \quad (12)$$

$$\cdot SO_4^- + H_2O \rightarrow HSO_4^- + \cdot OH \quad (13)$$

$^{\cdot}O_2^-$ is generated as described in eqn (14)–(17). Additionally, $^1O_2$, a selective ROS, may be produced *via* non-radical pathways. Its formation could result from the direct decomposition of PMS on the catalyst surface or through processes such as those outlined in eqn (18) and (19).

$$\cdot OH + \cdot OH \rightarrow H_2O_2 \quad (14)$$

$$\cdot OH + H_2O_2 \rightarrow \cdot HO_2^- \quad (15)$$

$$\cdot HO_2^- \rightarrow H^+ + \cdot O_2^- \quad (16)$$

$$O_2 + e^- \rightarrow \cdot O_2^- \quad (17)$$

$$\cdot O_2^- + 2H_2O \rightarrow {}^1O_2 + H_2O_2 + OH^- \quad (18)$$

$$HSO_5^- + SO_5^{2-} \rightarrow HSO_4^{2-} + SO_4^{2-} + {}^1O_2 \quad (19)$$

Finally, all ROS, including primary species such as $^{\cdot}O_2^-$ and $^1O_2$, as well as secondary species such as $^{\cdot}OH$ and $^{\cdot}SO_4^-$, collectively attack SMX, generating intermediates that are ultimately mineralized into CO_2 and H_2O (eqn (20)). The mechanism of SMX degradation by PMS activation on $MnCo_2S_4$/NF is shown in Fig. 6c.

$$\cdot SO_4^- + \cdot OH + \cdot O_2^- + {}^1O_2 + SMX \rightarrow \text{intermediates} \rightarrow CO_2 + H_2O \quad (20)$$

2.4 SMX degradation pathway and intermediates analysis

To elucidate the potential degradation pathways of SMX in the $MnCo_2S_4$/NF/PMS system, DFT calculations were employed to identify the reactive sites on the SMX molecule. The optimized SMX molecular geometry is presented in Fig. S9. The highest occupied molecular orbital (HOMO) was analyzed to determine regions with high electron density, which are more susceptible to electron loss and thus favorable sites for attack by electrophilic species (such as $^1O_2$).[42] The HOMO of SMX is primarily localized on the aromatic ring and sulfonamide group, suggesting that these regions, particularly the amino substituent on the benzene ring, are the most vulnerable to electrophilic attack (Fig. S10). This observation is also corroborated by the electrostatic potential (ESP) map, which also indicates that the sulfonamide moiety and aromatic ring possess the highest electron density (Fig. S11). While frontier molecular orbital theory and ESP distribution offer qualitative insights into regions prone to electron donation or acceptance, they lack atomic-level resolution regarding specific electrophilic and nucleophilic attack sites. To address this, we further analyzed the Fukui functions (f^-, f^+, f^0) to quantitatively assess the reactivity of individual atoms (Fig. S12–S14 and Table S9). The f^- values, which denote susceptibility to electrophilic attack, show N7, C2, C4, and C6 as the most reactive atoms, predominantly located on the aromatic ring. This suggests that the aromatic system plays a key role in reactions with electrophilic species $^1O_2$. These theoretical findings align well with quenching experiments and EPR analysis, which confirm $^1O_2$ as the dominant reactive species. Beyond electrophilic addition and electron abstraction by $^1O_2$, the potential for nucleophilic attack by superoxide radicals was also investigated. Analysis of f^+ values (indicative of nucleophilic susceptibility) reveals high reactivity at C1, C2, C3, C5, N7, and S8, located mainly within the aromatic and sulfonamide regions. These atoms are likely targets for $^{\bullet}O_2^-$ attack, potentially leading to hydroxylation or aromatic ring cleavage. The distribution of f^0 values, representing overall chemical reactivity, further emphasizes the aromatic ring as a central site for combining radical and non-radical oxidative processes. To enhance predictive accuracy and eliminate ambiguity in cases where a single atom may simultaneously exhibit high electrophilic and nucleophilic character, we also examined the condensed dual descriptor (CDD). Atoms with strongly negative CDD values (C2, C4, and N7) are identified as the most susceptible to electrophilic attack, whereas those with strongly positive values (C1 and S8) are more prone to nucleophilic attack. These results reinforce the view that SMX degradation in the $MnCo_2S_4$/NF/PMS system proceeds *via* a synergistic mechanism involving both non-radical $^1O_2$ and radical $^{\bullet}O_2^-$ species, each targeting specific atomic sites within the molecule.

High-performance liquid chromatography-mass spectrometry (HPLC-MS) was employed to identify the major intermediates generated during sulfamethoxazole (SMX) degradation, as summarized in Table S8. A total of nine potential degradation products were detected. Based on the identified intermediates and supported by DFT calculations, three plausible degradation pathways for SMX were proposed (Fig. S15). In pathway I, the amino group on the SMX molecule undergoes oxidation to form a nitroso derivative (P1, m/z = 268). Subsequent cleavage of the S–N bond in P1, induced by active oxidative species, leads to the formation of intermediate P3 (m/z = 300). P1 can also undergo further oxidation to produce P4 (m/z = 123), or it can undergo benzene ring cleavage to form P5 (m/z = 99). In pathway II, the S–N bond of SMX is directly cleaved, resulting in the formation of P7 (m/z =157) and P5 (m/z = 99). Similarly, pathway III yields P8 (m/z =149) and P9 (m/z =84) *via* oxidative fragmentation of the parent compound. Ultimately, these low-molecular-weight intermediates undergo further mineralization into CO_2, H_2O, and inorganic nitrogen species, achieving complete degradation of SMX. To evaluate the environmental impact of the detected intermediates, the Ecological Structure–Activity Relationship (ECOSAR) program was applied, a tool constructed on quantitative structure–activity relationship (QSAR) models.[43,44] As illustrated in Table S11, the acute toxicity (LC_{50}/EC_{50}) values of SMX were predicted to be 267 mg L^{-1} for fish, 6.43 mg L^{-1} for Daphnia, and 32.6 mg L^{-1} for green algae. According to the Globally Harmonized System (GHS) of classification and labelling of chemicals criteria, most identified intermediates displayed a reduction in acute and chronic toxicity. Although some degradation intermediates may temporarily increase ecological risk, the overall toxicity of the reaction system decreases during treatment. Therefore, degradation of SMX *via* the $MnCo_2S_4$/NF/PMS system not only facilitates efficient SMX removal but also reduces the overall ecological risk associated with SMX contamination.

2.5 Reusability and universality study

To assess the recyclability of the $MnCo_2S_4$/NF catalyst during PMS activation, SMX degradation tests were performed over seven consecutive PMS activation cycles (Fig. 7a). Even in the seven reuse cycles, the catalyst maintained over 82% SMX removal within 35 min, demonstrating minimal loss of activity. The slight decline in degradation performance over multiple cycles may result from incomplete regeneration of the catalyst. The persistent adsorption of degradation intermediates or residual organic fragments can lead to the competitive occupancy of active sites on the $MnCo_2S_4$. This localized blockage hinders the effective interaction between PMS molecules and the catalyst's metal centers, thereby leading to a reduction in the overall degradation kinetics. To assess the secondary pollution risk, the leaching of metal ions (Co, Mn, and Ni) was measured after the reaction. Analysis revealed that the concentrations of leached Co, Mn, and Ni were 0.047 mg L^{-1}, 0.023 mg L^{-1}, and 0.266 mg L^{-1} (Fig. S17), respectively, and remained well below the permissible limit of 1.0 mg L^{-1} according to the GB 25467-2010 (Discharge Standard of Pollutants for Municipal Wastewater Treatment Plant of China). In addition, XRD and SEM analyses were performed on the recovered catalyst after the reaction. The results show that the composition, structure, and morphology of the catalyst

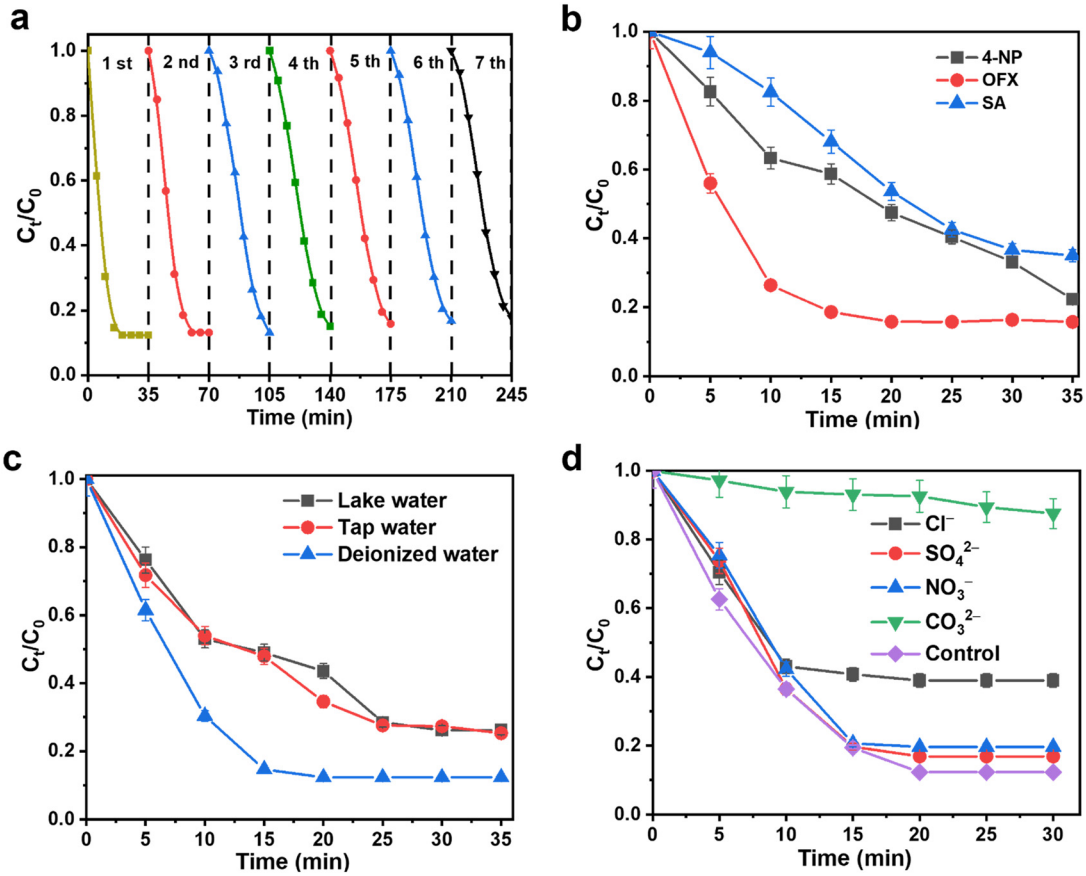

Fig. 7 (a) Cycling performance for SMX removal using $MnCo_2S_4$/NF/PMS systems; (b) performance of the $MnCo_2S_4$/NF/PMS system in degrading various organic pollutants; (c) SMX degradation efficiency under diverse water quality conditions; (d) influence of coexisting anions on SMX degradation.

remained largely unchanged before and after the reaction (Figs. S17 and S18). Thus, this cyclic performance highlights the excellent structural robustness of the $MnCo_2S_4$/NF composite and its sustained capacity to oxidatively degrade organic contaminants.

To demonstrate the broad applicability of the $MnCo_2S_4$/NF/PMS system, our degradation performance was evaluated against three representative organic contaminants, including 4-nitrophenol (4-NP), ofloxacin (OFX), and sulfonamide (SA). As shown in Fig. 7b, under identical conditions, all tested pollutants underwent rapid oxidative removal, achieving over 60% degradation within 35 minutes. Notably, OFX was degraded most efficiently, reaching 82% removal in the same time. These results show the universal efficacy of the catalyst and its potential for treating a wide range of recalcitrant organic compounds in water. The influence of different water matrices on the degradation of SMX by $MnCo_2S_4$/NF-activated PMS was illustrated in Fig. 7c and Table S12. In real water samples, the performance is partially inhibited, and the observed k_{obs} decreases from 0.1073 min^{-1} (in ultrapure water) to 0.0505 min^{-1} (in tap water) and 0.0421 min^{-1} (in lake water). This loss of activity is attributed to the presence of various anions and humic substances in tap and lake waters, which occupy active sites on the catalyst surface and scavenge free radicals, thus lowering the overall reaction efficiency. Despite this inhibition, $MnCo_2S_4$/NF-activated PMS still achieves a 75% removal of SMX in actual water, indicating its potential applicability for real-world water treatment.

Inorganic anions present in real wastewater can significantly influence the AOP by affecting three critical aspects, including the stability of the oxidant, the catalytic activity of the catalyst, and the degradation pathways of target pollutants. These interactions alter the production and reactivity of ROS, consequently impacting the efficiency of antibiotic degradation. Experimental evidence from Fig. 7d and Table S13 illustrates the effects of various inorganic anions on SMX degradation within the $MnCo_2S_4$/NF/PMS system. The results show that sulfate ions (SO_4^{2-}) exhibit a minimal inhibitory effect on SMX degradation. In contrast, other anions, such as chloride (Cl^-), nitrate (NO_3^-), and carbonate (CO_3^{2-}), react with $^{\bullet}OH$ and sulfate radicals $^{\bullet}SO_4^-$ to form less reactive inorganic radicals (eqn (21)–(25)). Among these, the addition of CO_3^{2-} generates carbonate radicals ($^{\bullet}CO_3^-$), which possess the lowest reactivity. This leads to the most pronounced inhibition of SMX degradation, as $^{\bullet}CO_3^-$ exhibits a reduced capacity to oxidize the pollutant.[37] This trend is further corroborated by the total organic carbon (TOC) analysis (Fig. S19). The control group without anions achieved a TOC removal of 49.7%, and the presence of SO_4^{2-}, NO_3^-, and

Cl^- slightly reduced the mineralization efficiency to 47.2%, 45.8%, and 42.7%, respectively. Most notably, the TOC removal sharply declined to 12.6% in the presence of CO_3^{2-}, indicating that the formation of $^{\cdot}CO_3^-$ not only slows down the primary degradation of SMX but also significantly hinders the deep oxidation of aromatic intermediates into CO_2 and H_2O.

$$\cdot OH + CO_3^{2-} \rightarrow OH^- + \cdot CO_3^- \quad (21)$$

$$\cdot SO_4^- + CO_3^{2-} \rightarrow SO_4^{2-} + \cdot CO_3^- \quad (22)$$

$$\cdot OH + Cl^- \rightarrow \cdot ClOH^- \quad (23)$$

$$\cdot SO_4^- + Cl^- \rightarrow SO_4^{2-} + \cdot Cl \quad (24)$$

$$\cdot SO_4^- + NO_3^- \rightarrow SO_4^{2-} + \cdot NO_3^- \quad (25)$$

3 Conclusions

In summary, this study successfully fabricated a 3D NF self-supported $MnCo_2S_4$ catalyst through an *in situ* growth strategy for the efficient activation of PMS toward SMX degradation. The $MnCo_2S_4$/NF achieved 87.7% SMX removal within 20 minutes and maintained over 82% efficiency after seven reuse cycles, indicating excellent stability. DFT calculations confirmed strong PMS adsorption on $MnCo_2S_4$/NF, promoting electron transfer and O–O bond cleavage. EPR analysis and quenching experiments demonstrate that both radical ($^{\cdot}O_2^-$) and non-radical ($^1O_2$) species synergistically serve as the primary active agents in SMX degradation. Fukui function analysis further revealed that SMX degradation proceeds with specific molecular sites (such as N7, C1, C5) showing high reactivity. The ecological risk of intermediates formed during SMX degradation was evaluated using the ECOSAR model, showing that most intermediates exhibited reduced toxicity compared to the parent compound. In addition to SMX, the $MnCo_2S_4$/NF/PMS system exhibited broad-spectrum degradation of other organic pollutants and sustained activity in real wastewater matrices, showing its practical potential. Future work could focus on scaling up the system and exploring its application to more complex industrial effluents for sustainable water treatment solutions.

4 Experimental section

4.1 Chemicals and materials

The chemical reagents used in the experiment are shown in the SI of Text S1.

4.2 Synthesis of $MnCo_2S_4$/NF

The nickel foam (NF, 1 cm × 1 cm, 1 cm × 2 cm, 1 cm × 3 cm) used in the experimental preparation was pretreated prior to use. It was sequentially immersed in hydrochloric acid (3 M), deionized water, and acetone, and ultrasonically cleaned in each solution for 10 min. Finally, the foam was rinsed three times with anhydrous ethanol and vacuum-dried at 60 °C for 2 h.

The Co/Mn-precursor was synthesized on the NF substrate *via* a hydrothermal method. Specifically, 1.164 g of $Co(NO_3)_2{\cdot}6H_2O$, 0.394 g of $MnCl_2{\cdot}4H_2O$, 0.37 g of NH_4F, and 0.72 g of urea were dissolved in 80 mL of distilled water and stirred magnetically for 30 min to ensure complete mixing. The pretreated nickel foam and the resulting solution were then transferred to a 100 mL Teflon-lined autoclave, which was maintained at 120 °C for 6 h. After cooling to room temperature, the sample was rinsed three times each with distilled water and ethanol to remove surface residues. The final product was denoted as Mn/Co-precursor/NF.

Subsequently, 0.2 g of thioacetamide was dissolved in 40 mL of distilled water and magnetically stirred for 15 min to ensure homogeneous mixing. The Co/Mn-precursor/NF and solution were sealed in a 100 mL Teflon-lined autoclave, heated at 120 °C for 3 h, cooled to room temperature, and washed three times with deionized water and ethanol. To enhance the crystallinity and structural stability of the material, the dried sample was transferred to a tube furnace, where it was heated to 700 °C at 5 °C min^{-1} and annealed for 1 hour in a N_2 environment. After natural cooling, the resulting catalyst was designated as $MnCo_2S_4$/NF.

4.3 Characterization

The details of the experimental characterization are presented in the SI of Text S2.

4.4 Experimental procedure and catalysis performance evaluation

A stock solution (200 mg L^{-1}) of sulfamethoxazole (SMX) was prepared by dissolving precise amounts of each in a 500 mL volumetric flask. Before the reaction, the pollutant solution was diluted to the desired concentration (20 mg L^{-1}, 100 mL). The solution was stirred at a constant temperature (30 °C, pH = 6) using a magnetic stirrer, followed by the sequential addition of the catalyst (1 × 2 cm^2) and peroxymonosulfate (PMS, 0.5 g L^{-1}) to the antibiotic solution. At intervals of 5 or 10 min, 1.5 mL of the reaction mixture was withdrawn using a syringe, filtered into a cuvette, and analyzed for concentration using a UV-vis spectrophotometer. The degradation efficiency (η) was calculated using the following equation:

$$\eta = \left(1 - \frac{C_t}{C_0}\right) \times 100\% \quad (26)$$

The degradation kinetics of antibiotic pollutants were modeled using a pseudo-first-order kinetic equation, with the apparent rate constant (k_{obs}) determined according to the following equation:

$$\ln\left(\frac{C_t}{C_0}\right) = -k_{obs}t \quad (27)$$

Considering the heterogeneous nature of the $MnCo_2S_4$/NF/PMS system, where the reaction occurs on the catalyst surface, the

Langmuir–Hinshelwood (L–H) model was further employed to describe the degradation kinetics:

$$\frac{\ln\left(\frac{C_0}{C_t}\right)}{C_0 - C_t} = k_r K_{ads} \frac{t}{C_0 - C_t} - K_{ads} \quad (28)$$

To investigate the temperature dependence of the reaction, multiple sets of comparative experiments were conducted under identical conditions but at varying temperatures. The apparent activation energy (E_a, kJ mol^{-1}) was calculated using the Arrhenius equation:

$$\ln k = \ln A - E_a/RT \quad (29)$$

where t is the reaction time (min), C_0 is the initial concentration of the antibiotic pollutant (mg L^{-1}), and C_t is the concentration at sampling time (mg L^{-1}), k_r is the intrinsic reaction rate constant (mg L^{-1} min^{-1}), K_{ads} represents the adsorption coefficient (L mg^{-1}), A is the pre-exponential factor, R is the universal gas constant (8.314 J mol^{-1} K^{-1}), and T is the absolute temperature (K).

Additional factors influencing degradation performance, along with detailed experimental protocols for active oxygen investigations and cyclic performance assessments, are comprehensively described in the Texts S3–S6. The performance evaluations were conducted using UV-visible spectrophotometry, as described in the SI of Text S7.

4.5 Theoretical calculation

Computational specifics are provided in the SI of Text S8.

Author contributions

Mengqing Hu: validation, data curation, software, writing - original draft, and writing - review & editing. Di Zhao: investigation, data curation, software, and writing - review & editing. Xinlong Yan: methodology, conceptualization, supervision, writing - review & editing, and funding acquisition. Xiaoyan Hu: writing - review & editing. Xiaofeng Jiang: investigation. Shiwei Yin: software. Ming Zhou: writing - review & editing. Yun Wang: Supervision, software, and writing - review & editing.

Conflicts of interest

The authors declare no conflict of interest.

Data availability

All experimental data supporting the conclusions of this study are available in the main text and supplementary information (SI).

Supplementary information is available. See DOI: https://doi.org/10.1039/d6im00026f.

Acknowledgements

This work was supported by the National Natural Science Foundation of China (No. 22378417) and the Priority Academic Program Development of Jiangsu Higher Education Institutions, China.

References

1 A. Singh, S. G. Pratap and A. Raj, Occurrence and dissemination of antibiotics and antibiotic resistance in aquatic environment and its ecological implications: A review, *Environ. Sci. Pollut. Res.*, 2024, **31**, 47505–47529.
2 S. Rodriguez-Mozaz, S. Chamorro, E. Marti, B. Huerta, M. Gros, A. Sànchez-Melsió, C. M. Borrego, D. Barceló and J. L. Balcázar, Occurrence of antibiotics and antibiotic resistance genes in hospital and urban wastewaters and their impact on the receiving river, *Water Res.*, 2015, **69**, 234–242.
3 A. Wang, Y.-Y. Li and A. L. Estrada, Mineralization of antibiotic sulfamethoxazole by photoelectro-Fenton treatment using activated carbon fiber cathode and under UVA irradiation, *Appl. Catal., B*, 2011, **102**, 378–386.
4 D. Archundia, C. Duwig, L. Spadini, M.-C. Morel, B. Prado, M. Perez, V. Orsag and J. M. Martins, Assessment of the sulfamethoxazole mobility in natural soils and of the risk of contamination of water resources at the catchment scale, *Environ. Int.*, 2019, **130**, 104905.
5 S.-F. Yang, C.-F. Lin, C.-J. Wu, K.-K. Ng, A. Y.-C. Lin and P.-K. A. Hong, Fate of sulfonamide antibiotics in contact with activated sludge–sorption and biodegradation, *Water Res.*, 2012, **46**, 1301–1308.
6 A. Sochacki, K. Kowalska, E. Felis, S. Bajkacz, J. Kalka, A. Brzeszkiewicz, Z. Vaňková and A. Jakóbik-Kolon, Removal and transformation of sulfamethoxazole in acclimated biofilters with various operation modes-Implications for full-scale application, *Chemosphere*, 2021, **280**, 130638.
7 D. T. Oyekunle, E. A. Gendy, J. Ifthikar and Z. Chen, Heterogeneous activation of persulfate by metal and non-metal catalyst for the degradation of sulfamethoxazole: A review, *Chem. Eng. J.*, 2022, **437**, 135277.
8 F. Wang, H. Fu, F.-X. Wang, X.-W. Zhang, P. Wang, C. Zhao and C.-C. Wang, Enhanced catalytic sulfamethoxazole degradation via peroxymonosulfate activation over amorphous CoSx@SiO_2 nanocages derived from ZIF-67, *J. Hazard. Mater.*, 2022, **423**, 126998.
9 Z. Chen, X. Huang, Y. Zuo, H. Wang, W. Chen, L. Kong and X. Lin, High-entropy perovskite embedded in carbon-based catalyst toward peroxymonosulfate activation to degrade Rhodamine B: Performance and mechanism insights, *Water Res.*, 2025, 123919.
10 M. Hu, D. Zhao, X. Yan, Y. Wang, J. Zhang, X. Hu, M. Zhou and P. Liu, Enhanced peroxymonosulfate activation for antibiotic and heavy metal removal using ZIF-67-derived magnetic Ni/Co-LDH@NC: Bimetallic electronic synergy and oxygen vacancy effects, *Appl. Catal., B*, 2025, **362**, 124753.

11 Y. Gao, T. Wu, C. Yang, C. Ma, Z. Zhao, Z. Wu, S. Cao, W. Geng, Y. Wang and Y. Yao, Activity trends and mechanisms in peroxymonosulfate-assisted catalytic production of singlet oxygen over atomic metal-N-C catalysts, *Angew. Chem., Int. Ed.*, 2021, **60**, 22513–22521.

12 S. Liu, Z. Zhang, F. Huang, Y. Liu, L. Feng, J. Jiang, L. Zhang, F. Qi and C. Liu, Carbonized polyaniline activated peroxymonosulfate (PMS) for phenol degradation: Role of PMS adsorption and singlet oxygen generation, *Appl. Catal., B*, 2021, **286**, 119921.

13 X. Zheng, X. Niu, D. Zhang, M. Lv, X. Ye, J. Ma, Z. Lin and M. Fu, Metal-based catalysts for persulfate and peroxymonosulfate activation in heterogeneous ways: A review, *Chem. Eng. J.*, 2022, **429**, 132323.

14 X. Duan, J. Kang, W. Tian, H. Zhang, S.-H. Ho, Y.-A. Zhu, Z. Ao, H. Sun and S. Wang, Interfacial-engineered cobalt@carbon hybrids for synergistically boosted evolution of sulfate radicals toward green oxidation, *Appl. Catal., B*, 2019, **256**, 117795.

15 Y. Gao, Y. Zhou, S.-Y. Pang, J. Jiang, Y.-M. Shen, Y. Song, J.-B. Duan and Q. Guo, Enhanced peroxymonosulfate activation via complexed Mn (II): A novel non-radical oxidation mechanism involving manganese intermediates, *Water Res.*, 2021, **193**, 116856.

16 J. Ali, S. Guo, Y. Chen, A. Shahzad, M. W. Ullah and F. Chen, Metal sulfides as emerging materials for advanced oxidation of wastewater: Recent developments, challenges, and prospects, *Coord. Chem. Rev.*, 2024, **509**, 215765.

17 Z. Zhao, L. Lin, S. Liu, Y. Chen, S. V. Daniels, Z. Xu, Z. Chen, H. Li, Y. Wu and L. Guo, Unveiling the versatile performance of transition metal sulfides in peroxymonosulfate activation, *Chem. Eng. J.*, 2024, **497**, 154682.

18 T. Sun, C.-x. Li, Y.-p. Bao, J. Fan and E. Liu, S-scheme $MnCo_2S_4$/g-C_3N_4 heterojunction photocatalyst for H_2 production, *Acta Phys.-Chim. Sin.*, 2023, **39**, 2212009.

19 J. Hou, X. He, S. Zhang, J. Yu, M. Feng and X. Li, Recent advances in cobalt-activated sulfate radical-based advanced oxidation processes for water remediation: A review, *Sci. Total Environ.*, 2021, **770**, 145311.

20 W. Li, Y. Xu, D. Zhong, D. Tang, T. Xiang, C. Fan and Y. Yang, Efficient activation of peroxymonosulfate for degradation of rhodamine B by anchoring $CoFe_2O_4$ on MoS_2 nanoflower-modified biochar, *Langmuir*, 2025, **41**, 6903–6919.

21 X. Han, W. Zhang, S. Li, C. Cheng, Q. Yu, Q. Jia, L. Zhou and G. Xiu, Mn-MOF derived manganese sulfide as peroxymonosulfate activator for levofloxacin degradation: An electron-transfer dominated and radical/nonradical coupling process, *J. Environ. Sci.*, 2023, **130**, 197–211.

22 S. Lawson, X. Li, H. Thakkar, A. A. Rownaghi and F. Rezaei, Recent advances in 3D printing of structured materials for adsorption and catalysis applications, *Chem. Rev.*, 2021, **121**, 6246–6291.

23 H. Zhao, X. Xu, W. Cui, L. Geng, X. Peng, J. Yang, X. Shao and Y. Liu, Synchronization strategy for activity and stability in Fenton-like single-atom catalysis, *Adv. Mater.*, 2025, 2503217.

24 L. Song, X. Cheng, Y. Yang, Y. Hou, X. Gan, C. Wang and J. Shang, In-situ growth of Mn_2O_3/$MnCo_2O_4$ on 3D nickel foam as a novel heterogeneous composites peroxymonosulfate activator for the degradation of levofloxacin: Performance, stability and mechanism, *Chem. Eng. J.*, 2023, **471**, 144629.

25 E. G. Neiva, M. M. Oliveira, L. H. Marcolino Jr and A. J. Zarbin, Nickel nanoparticles with hcp structure: Preparation, deposition as thin films and application as electrochemical sensor, *J. Colloid Interface Sci.*, 2016, **468**, 34–41.

26 M. A. Raza, N. Iqbal, T. Noor and Z. A. Ghazi, Hierarchical flower-like NiMn-LDH@$MnCo_2S_4$ grown on nickel foam as a high-specific capacity faradaic electrode, *Energy Fuels*, 2022, **37**, 1310–1317.

27 B. Hou, J. Fu, H. Su and X. Du, Preparation of 3D nanostructured $MnCo_2S_4$ as a robust electrocatalyst for overall water splitting, *ChemistrySelect*, 2019, **4**, 4499–4505.

28 N. A. Jarrah, F. Li, J. G. van Ommen and L. Lefferts, Immobilization of a layer of carbon nanofibres (CNFs) on Ni foam: A new structured catalyst support, *J. Mater. Chem.*, 2005, **15**, 1946–1953.

29 J. Luo, S. Bo, Q. An, Z. Xiao, H. Wang, W. Cai, S. Zhai and Z. Li, Designing ordered composites with confined Co-N/C layers for efficient pollutant degradation: Structure-dependent performance and PMS activation mechanism, *Microporous Mesoporous Mater.*, 2020, **293**, 109810.

30 J. Li, Z. Li, F. Ning, L. Zhou, R. Zhang, M. Shao and M. Wei, Ultrathin mesoporous Co_3O_4 nanosheet arrays for high-performance lithium-ion batteries, *ACS Omega*, 2018, **3**, 1675–1683.

31 S. Cheng, Y. Liu, X. Liu, C. Zhu, J. Luo, J. Cao and F. Liu, Co_3O_4 nanosheets modified by Ni@C nanoparticles as effective flow-through electrode for electro-activation of PMS: Ni@C as electron shuttle for accelerated Co^{3+}/Co^{2+} cycle in bulk Co_3O_4, *Chem. Eng. J.*, 2023, **472**, 145084.

32 D. Shen, R. Zhang, Y. Ma, J. Niu, D. Xia, Y. Yang, Z. Ren, Y. Song, S. Wei and W. Dong, Regulation of sulfurization degree: A strategy to improve the electrochemical performance of $MnCo_2O_4$@$MnCo_2S_4$ composites in supercapacitors, *Chem. Eng. J.*, 2025, **513**, 162819.

33 M. Hu, D. Zhao, M. Dong, H. Q. Fu, Y. Zou, Y. Xu, M. Zhou, L. Zhang, L. Wang and Y. Shu, Three-dimensional porous Ti supported Ni/Sb Co-doped SnO_2 anode for electrocatalytic production of ozone, *J. Environ. Chem. Eng.*, 2024, **12**, 114915.

34 D. Escalera-López, Y. Niu, S. J. Park, M. Isaacs, K. Wilson, R. E. Palmer and N. V. Rees, Hydrogen evolution enhancement of ultra-low loading, size-selected molybdenum sulfide nanoclusters by sulfur enrichment, *Appl. Catal., B*, 2018, **235**, 84–91.

35 R. He, X. Huang and L. Feng, Recent progress in transition-metal sulfide catalyst regulation for improved oxygen evolution reaction, *Energy Fuels*, 2022, **36**, 6675–6694.

36 W. Li, Q. Zhu, X. Yin, Z. Gao, K. Wei, S. Liu, X. Zhang, H. Chen, Y. Zhang and W. Han, Enhanced heterogeneous Fenton catalysis by carbon nanotube-loaded Mn doped FeS_2 catalysts for pollutant degradation: Co-enhancement effect of Fe-S-Mn and Fe-SC linkages, *Sep. Purif. Technol.*, 2024, **335**, 126150.

37 M. P. Rayaroth, G. Boczkaj, O. Aubry, U. K. Aravind and C. T. Aravindakumar, Advanced oxidation processes for degradation of water pollutants—ambivalent impact of carbonate species: A review, *Water*, 2023, **15**, 1615.

38 H. Zhang, C. Xie, L. Chen, J. Duan, F. Li and W. Liu, Different reaction mechanisms of $SO_4^{\bullet-}$ and $^{\bullet}OH$ with organic compound interpreted at molecular orbital level in Co(II)/peroxymonosulfate catalytic activation system, *Water Res.*, 2023, **229**, 119392.

39 H. Xu, M. Zhang, Q. Zhang, J. Wu, X. Zhou, J. Zhang, F. Hao, Z. Liu, L. Sheng and Y. Tang, Active edge sites engineering on amorphous Co-Mn spinel-based oxides for efficient peroxymonosulfate activation, *Angew. Chem., Int. Ed.*, 2025, e202509527.

40 Y. Yao, C. Wang, Y. Yang, S. Zhang, X. Yan, C. Xiao, Y. Zhou, Z. Zhu, J. Qi and X. Sun, Mn-Co dual sites relay activation of peroxymonosulfate for accelerated decontamination, *Appl. Catal., B*, 2023, **330**, 122656.

41 M. Zhao, W. Li, J. Li, W. Hu and C. M. Li, Strong electronic interaction enhanced electrocatalysis of metal sulfide clusters embedded metal–organic framework ultrathin nanosheets toward highly efficient overall water splitting, *Adv. Sci.*, 2020, **7**, 2001965.

42 V. Choudhary, A. Bhatt, D. Dash and N. Sharma, DFT calculations on molecular structures, HOMO-LUMO study, reactivity descriptors and spectral analyses of newly synthesized diorganotin(IV) 2-chloridophenylacetohydroxamate complexes, *J. Comput. Chem.*, 2019, **40**, 2354–2363.

43 T. I. Netzeva, M. Pavan and A. P. Worth, Review of (quantitative) structure–activity relationships for acute aquatic toxicity, *QSAR Comb. Sci.*, 2008, **27**, 77–90.

44 Y. Yang, X. Lu, J. Jiang, J. Ma, G. Liu, Y. Cao, W. Liu, J. Li, S. Pang and X. Kong, Degradation of sulfamethoxazole by UV, UV/H_2O_2 and UV/persulfate (PDS): Formation of oxidation products and effect of bicarbonate, *Water Res.*, 2017, **118**, 196–207.